

The VIMOS Public Extragalactic Survey (VIPERS) ★

First Data Release of 57 204 spectroscopic measurements

B. Garilli¹, L. Guzzo^{2,3}, M. Scodreggio¹, M. Bolzonella⁹, U. Abbas⁵, C. Adami⁴, S. Arnouts^{6,4}, J. Bel⁷, D. Bottini¹, E. Branchini^{10,27,28}, A. Cappi⁹, J. Coupon¹², O. Cucciati^{9,17}, I. Davidzon^{9,17}, G. De Lucia¹³, S. de la Torre¹⁴, P. Franzetti¹, A. Fritz¹, M. Fumana¹, B. R. Granett², O. Ilbert⁴, A. Iovino², J. Krywult¹⁵, V. Le Brun⁴, O. Le Fèvre⁴, D. Maccagni¹, K. Małek¹⁶, F. Marulli^{17,18,9}, H. J. McCracken¹⁹, L. Paioro¹, M. Polletta¹, A. Pollo^{21,22}, H. Schlegelhauser^{23,20}, L. A. M. Tasca⁴, R. Tojeiro¹¹, D. Vergani²⁴, G. Zamorani⁹, A. Zanichelli²⁵, A. Burden¹¹, C. Di Porto⁹, A. Marchetti^{2,26}, C. Marinoni⁷, Y. Mellier¹⁹, L. Moscardini^{17,18,9}, R. C. Nichol¹¹, J. A. Peacock¹⁴, W. J. Percival¹¹, S. Phleps²⁰, and M. Wolk¹⁹

(Affiliations can be found after the references)

Received ...; accepted ...

ABSTRACT

We present the first Public Data Release (PDR-1) of the VIMOS Public Extragalactic Survey (VIPERS). It comprises 57 204 spectroscopic measurements together with all additional information necessary for optimal scientific exploitation of the data, in particular the associated photometric measurements and quantification of the photometric and survey completeness. VIPERS is an ESO Large Programme designed to build a spectroscopic sample of $\approx 100\,000$ galaxies with $i_{AB} < 22.5$ and $0.5 < z < 1.5$ with high sampling rate ($\approx 45\%$). The survey spectroscopic targets are selected from the CFHTLS-Wide five-band catalogues in the W1 and W4 fields. The final survey will cover a total area of nearly 24 deg^2 , for a total comoving volume between $z = 0.5$ and 1.2 of $\approx 4 \times 10^7 h^{-3}\text{Mpc}^3$ and a median galaxy redshift of $z \approx 0.8$. The release presented in this paper includes data from virtually the entire W4 field and nearly half of the W1 area, thus representing 64% of the final dataset. We provide a detailed description of sample selection, observations and data reduction procedures; we summarise the global properties of the spectroscopic catalogue and explain the associated data products and their use, and provide all the details for accessing the data through the survey database (<http://vipers.inaf.it>) where all information can be queried interactively.

Key words. Galaxies: distances and redshifts – Galaxies: statistics – Galaxies: fundamental parameters – Cosmology: observations – Cosmology: large-scale structure of the Universe – Astronomical databases: Catalogues

1. Introduction

The VIMOS Public Extragalactic Redshift Survey (VIPERS; Guzzo et al. 2013) has been designed to measure redshifts for approximately 100 000 galaxies with $i_{AB} < 22.5$ in the range $0.5 < z < 1.5$. The general aim of the project is to build a sample of the global galaxy population that matches in several respects those available locally ($z < 0.2$) from the large redshift surveys of the past decade, namely the 2dFGRS (Colless et al. 2001) and SDSS (Abazajian et al. 2003) surveys, thus allowing combined evolutionary studies of both galaxy physical and clustering properties, on a comparable statistical footing. Building

upon the experience and results of previous VIMOS surveys (Le Fèvre et al. (2005), Lilly et al. (2007)) VIPERS provides a detailed and representative picture of the whole galaxy population and its large-scale structure when the Universe was about half its current age, representing nearly an order of magnitude improvement in terms of volume and number of galaxies over previous surveys of this type (see Guzzo et al. (2013) for a more detailed introduction in the context of cosmological surveys). The main goals of VIPERS are:

1. To measure the clustering of galaxies at $\langle z \rangle \approx 0.8$ on scales up to $\sim 100\text{ Mpc } h^{-1}$, in order to:

- extract cosmological information from the large-scale shape of the power spectrum (Bel et al. 2013; Granett et al. 2012; Xia et al. 2012);
- quantify the dependence of galaxy clustering on galaxy physical properties (such as luminosity and stellar mass) and its evolution with time (Marulli et al. 2013);
- quantify the mean galaxy occupation of dark matter halos using small/intermediate-scale clustering and its time evolution;
- study the halo occupation distribution (HOD) using a combination of galaxy-galaxy lensing, galaxy clustering and stellar mass functions (Coupon et al., in preparation);
- measure higher-order clustering statistics and characterize the non-linear development of clustering over the past 7 billion years.

Send offprint requests to: B. Garilli, bianca@lambrate.inaf.it

* based on observations collected at the European Southern Observatory, Cerro Paranal, Chile, using the Very Large Telescope under programs 182.A-0886 and partly 070.A-9007. Also based on observations obtained with MegaPrime/MegaCam, a joint project of CFHT and CEA/DAPNIA, at the Canada-France-Hawaii Telescope (CFHT), which is operated by the National Research Council (NRC) of Canada, the Institut National des Sciences de l'Univers of the Centre National de la Recherche Scientifique (CNRS) of France, and the University of Hawaii. This work is based in part on data products produced at TERAPIX and the Canadian Astronomy Data Centre as part of the Canada-France-Hawaii Telescope Legacy Survey, a collaborative project of NRC and CNRS. The VIPERS web site is <http://vipers.inaf.it/>.

2. To measure, at the same redshifts, the growth rate of structure using redshift-space distortions in the observed clustering (de la Torre et al. 2013), in particular exploiting the broad population and high spatial sampling of VIPERS through the use of multiple tracers of the underlying mass density field.

3. To precisely characterise the galaxy population at $\langle z \rangle \approx 0.8$ in terms of the distributions of fundamental properties such as luminosity, colours and stellar mass, tracing their evolution with cosmic time (Davidzon et al. 2013; Fritz et al. 2013).

4. To reconstruct the density field at $\langle z \rangle \approx 0.8$ in order to:

(a) determine the bias parameter and its evolution $b(z)$ (Branchini et al., in preparation);

(b) quantify at these redshifts the relationship between galaxy properties and local environment, elucidating the role of mass and environment in the evolution of galaxies.

5. To provide the community with an unprecedented spectroscopic database at $0.5 < z < 1.5$, including extensive information on galaxy physical properties. The latter is made possible by combining the spectral information with the CFHTLS five-band magnitudes on which the survey is based¹ (Goranova et al. 2009), plus additional ancillary data in the UV and infrared bands (GALEX, UKIDSS, VISTA, SWIRE, VLA, XMM-LSS), enabling to derive Spectral Energy Distribution information (Marchetti et al. 2013, Davidzon et al. 2013) and automatic galaxy/AGN/stellar classification (Małek et al. 2013).

Although carried out within the standard (proprietary) scheme of the ESO Large Programmes, VIPERS was conceived from its start as a public survey, with the clear idea that the range of science that will be performed by the community should greatly exceed the core analyses described above. The set of data that is described in this paper and made public with the VIPERS Public Data Release 1 (PDR-1), is the same used for all papers of the first VIPERS science release of March 2013. Several aspects of the survey construction and the data are also discussed in Guzzo et al. (2013) and are only briefly summarised here.

The layout of the paper is as follows: §2 summarises the survey strategy and design; §3 describes the VLT-VIMOS observations; §4 discusses the data reduction, including redshift estimation and quality tests; §5 presents the PDR-1 sample, discussing redshift errors and comparison to external data; §6 describes the survey masks and discusses in detail the selection effects that need to be taken into account for a proper use of the PDR-1 data; §7 provides a first look at the VIPERS spectra, including a brief preliminary discussion of trends and correlations spectral features and galaxy classification schemes; §8 provides information on the data access in the VIPERS data base; finally, §9 provides a brief summary.

2. Survey strategy and design

2.1. Star-galaxy separation and target definition

VIPERS was conceived in 2007, focusing on the study of clustering and redshift-space distortions at $z \approx 0.5 - 1.2$, but with a desire to enable broader goals involving large-scale structure and galaxy evolution. The survey design was also strongly driven by the specific features of the VIMOS spectrograph, which has a relatively small field of view compared to fibre-fed instruments ($\approx 18 \times 16$ arcmin²), but a larger yield in terms of redshifts per unit area (up to 1000 spectra per exposure: Le Fèvre et al. 2003).

The VIPERS overall sky coverage and field layout is shown in Figure 1; the solid red line delimits the planned area, while the

black dots show the spectroscopically observed objects. Table 1 shows the area planned in each of the two survey fields as well as the area already spectroscopically covered, which is the subject of the current data release. The effective area is computed taking into account only those portions of sky effectively exposed, i.e. not considering failed quadrants and the dead cross between VIMOS quadrants. The last column in Table 1 gives the area where photometry is reliable (see Section 6.1). Given the luminosity function of galaxies and results from previous VIMOS surveys (VVDS Deep and Wide: Le Fèvre et al. 2005; Garilli et al. 2008; zCOSMOS: Lilly et al. 2009), it was known that a magnitude-limited sample with $i_{AB} < 22.5$ would cover the redshift range out to $z \sim 1.2$, and could be assembled with fairly short VIMOS exposure times (< 1 hour). Also, taking 2dFGRS as a local reference, a survey volume around $5 \times 10^7 h^{-3} \text{Mpc}^3$ could be explored by observing an area of $\approx 24 \text{ deg}^2$.

Building upon this experience, VIPERS was designed to maximize the number of galaxies observed in the range of interest, i.e. at $z > 0.5$, while at the same time attempting to select against stars that represented a contamination of up to 30% in some of the VVDS-Wide fields (where by design no star-galaxy separation whatsoever had been applied: see Garilli et al. 2008). Therefore we searched for a criterion that could limit the stellar contamination without hampering the completeness of the galaxy sample.

Stars and galaxies were separated using both their measured size and their spectral energy distribution, derived through template fitting of the high-quality CFHTLS 5-band photometry. As shown by the extensive tests carried out using the fully sampled VVDS (Deep and Wide) data, the overall galaxy completeness and resulting stellar contamination can be optimized by applying the following criteria (Guzzo et al. 2013):

1. At $i_{AB} < 21$, stars are defined to be objects with $r_h < \mu_{rh} + 3\sigma_{rh}$. Galaxies are the complementary class.
2. At $i_{AB} \geq 21$, the previous criterion would exclude small compact galaxies from the target sample. For these reason, objects are discarded as *bona fide* stars if $r_h < \mu_{rh} + 3\sigma_{rh}$ AND $\log_{10}(\chi_{\text{star}}^2) < \log_{10}(\chi_{\text{gal}}^2) + 1$,

where r_h is the half-light radius of an object; μ_{rh} and σ_{rh} are the mean and standard deviation of the r_h distribution; while χ_{star}^2 and χ_{gal}^2 result from the spectral energy distribution template fitting applied to the CFHTLS photometry.

The desired redshift range ($z > 0.5$) for the objects classified as galaxies is then selected requiring that

$$(r - i) > 0.5(u - g) \quad \vee \quad (r - i) > 0.7 \quad (1)$$

(see Figure 3 in Guzzo et al. 2013).

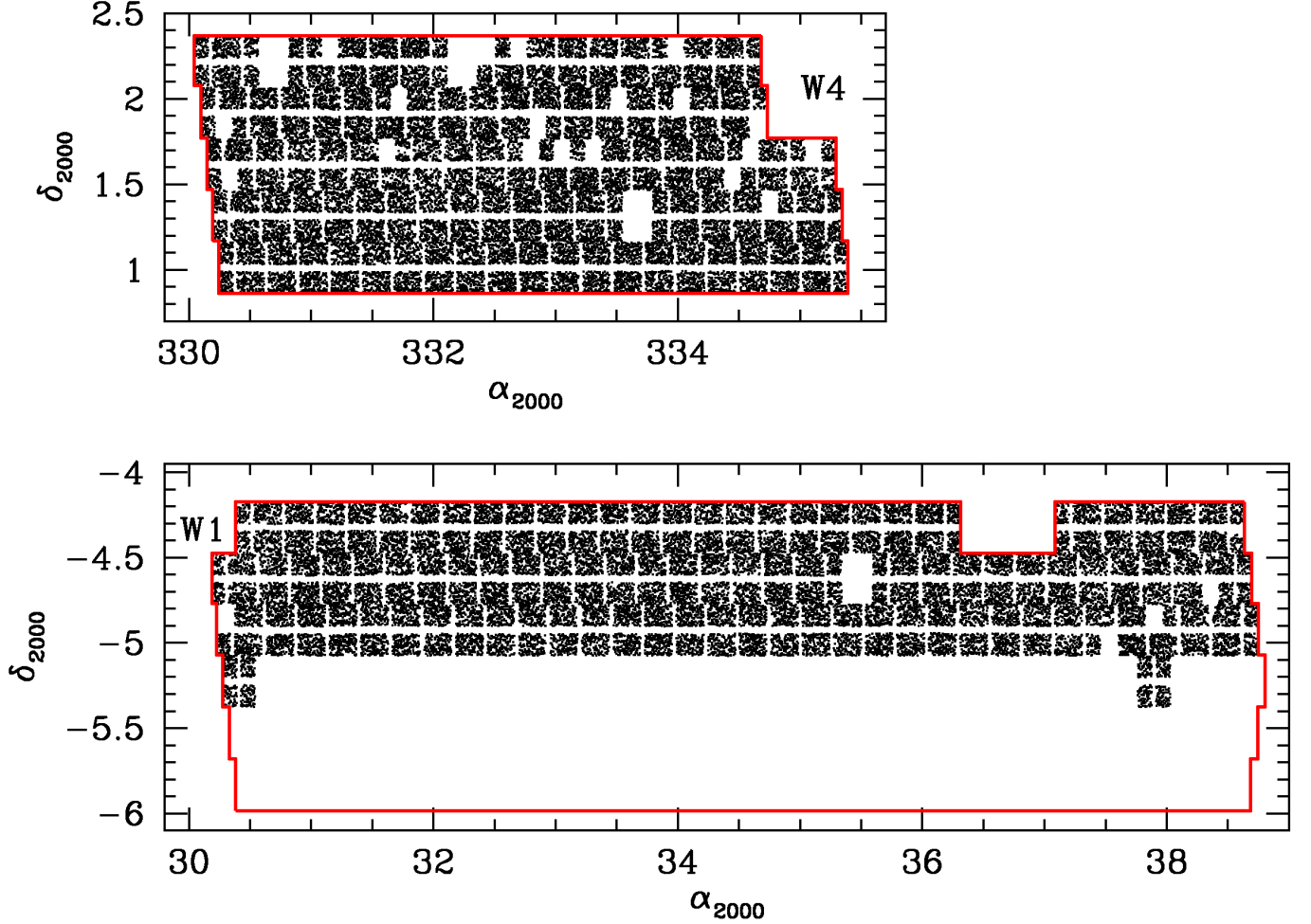
2.2. Additional AGN targets

To broaden the scientific yield of the project, without affecting the purity of the galaxy selection function, it was also decided to supplement the target list with a small number of AGN (Active Galactic Nuclei) candidates: (1) a set of 449 X-ray selected candidates from the XMM-LSS survey in the W1 field (Pierre et al. 2007), supplied by the XMM-LSS Consortium and added as compulsory targets (average of one object every two quadrants); and (2) a set of 3696 photometrically defined AGN candidates, selected among stellar objects resulting from the previous star-galaxy separation. In a first version, an object was classi-

¹ <http://www.cfht.hawaii.edu/Science/CFHTLS/>

Table 1. VIPERS survey field positions and area coverage: Surveyed area is the total area on sky, effective area is net of VIMOS cross and failed pointings/quadrants.

Field	R.A. ¹	Dec ¹	Final surveyed area	PDR-1 surveyed area	PDR-1 effective area	PDR-1 area with good photometry
0226 – 04 (W1)	02h26m00.0s	–04deg30′00″	15.701 deg ²	7.932 deg ²	5.478 deg ²	5.347 deg ²
2217 + 00 (W4)	22h17m50.4s	+00deg24′00″	7.851 deg ²	7.851 deg ²	5.120 deg ²	4.968 deg ²

¹ Center of Field

Fig. 1. VIPERS survey areas. Black areas are the spectroscopically observed pointings. The thick red line delimits the full area at the survey end. In the current release, some holes due to bad observing conditions are present. Some of them will be filled before the end of the survey.

fied as an AGN candidate if its colours satisfied the following criteria:

$$\text{CC1} : \begin{cases} (g-r) < 1 \wedge (u-g) < 0.6 \\ (g-r) < 1 \wedge 0.6 \leq (u-g) < 1.2 \\ \quad \wedge (g-r) > 0.5(u-g) + 0.036 \\ (g-r) < 1 \wedge 0.6 \leq (u-g) < 2.6 \\ \quad \wedge (g-r) < 0.5(u-g) + 0.214 \\ (g-r) < 1 \wedge (u-g) > 2.6. \end{cases} \quad (2)$$

These criteria were calibrated on the VVDS point-like objects brighter than $i_{AB} = 21$, and we expected a sample with a completeness of 87.5% and with a stellar contamination of 36%. These percentages were not confirmed by the actual data at the end of the first observing season, indicating a significantly higher than expected contamination from stars. While investigating the

origin of this discrepancy, we decided to revise criteria towards a more restrictive definition, following which an AGN candidate must satisfy equation 2 and :

$$\text{CC2} : \begin{cases} (u-g) < 0.6 \wedge -0.2 < (g-i) < 1 \\ 0.6 \leq (u-g) < 1 \wedge -0.2 < (g-i) < 0.2 \\ (u-g) \geq 1 \wedge (g-i) < 0.6. \end{cases} \quad (3)$$

This more stringent definition has been applied in all observations from 2010 onwards.

AGN redshifts from photometrically defined candidates are included in the released catalogue, but the precise selection function to correct for any incompleteness is still being verified. Brighter than $i_{AB} = 21$, where our selection for point-like AGN had been tested, the number counts of the AGN candidates and the confirmation rate are as expected. Fainter than that, where AGN have been observed as part of the primary target sample,

the selection function changes. A complete analysis of the sample of spectroscopically confirmed AGN will be the subject of a separate paper. The 189 XMM-LSS AGN candidates observed so far are not included in PDR-1, and will be analysed separately.

3. VLT-VIMOS Observations

The VIPERS survey is being performed in the framework of the ESO Large programmes and is carried out using VIMOS on ‘Melipal’, the Very Large Telescope (VLT) Unit 3 (Le Fèvre et al. 2003). VIMOS (Visible Imager Multi Object Spectrograph) makes use of slits cut out from masks. Its field of view of $\approx 18 \times 16$ arcmin² is divided into four quadrants, each having an area of $\approx 7 \times 8.1$ arcmin². Each quadrant corresponds to an independent spectrograph and the four spectrographs observe in the same configuration for the same exposure time.

The standard VIMOS observing procedure requires the acquisition of a direct image, which is used for mask preparation with the *vmmps* software (Bottini et al. 2005) distributed by ESO: *vmmps* assigns the slit length taking into account object dimensions and sky subtraction regions as specified by the user. The minimum slit length can be changed by the software as part of the optimization process, to maximize the number of slits per quadrant. The files containing the mask definition are sent to ESO (via the P2PP tool) for mask cutting before spectroscopic observations. As VIMOS suffers from some flexure problems, calibration exposures are performed immediately after the scientific exposures, maintaining the instrument at the same rotation angle as the scientific exposure and inserting a screen at the Nasmit focus. This ensures that we have calibration lamps with the same flexure-induced distortions as the scientific images, thus allowing for a more precise wavelength calibration. The instrument has no atmospheric dispersion compensator; in order to avoid spectra distortions due to atmospheric refraction, observations are confined within ± 2 hours from the meridian.

Given the chosen magnitude limit ($i_{AB} \leq 22.5$), the total exposure time adopted for the VIPERS spectroscopic observations is 2700 sec. The observation of one pointing is split into five exposures of nine minutes each. Observations have been carried out aligning slits along the East-West direction, so that atmospheric refraction effects are minimized. We use 1-arcsec wide slits, a value which well matches the average seeing in Paranal. The ‘Low-Resolution Red’ (LR-Red) grism is used, providing a spectral resolution $R \approx 230$ and a mean dispersion of $7.3 \text{ \AA}/\text{pixel}$. When preparing masks, we have allowed for a minimum of 1.8 arcsec per side for sky subtraction. In order to further boost the survey sampling and the multiplexing capabilities of VIMOS, we have followed the approach described in Scodreggio et al. (2009): essentially, we have arbitrarily assigned an object size of 0.5 arcsec to all VIPERS sources. In this way, *vmmps* has more freedom in the slit positioning optimization process, and we have been able to increase the number of objects per quadrant by $\sim 10\%$, reaching a median of 87 slits per quadrant (see Figure 2). The drawback of this approach is that bigger objects have a non-negligible chance of filling most of the slit, and sometimes the automatic spectral extraction may fail. *A posteriori* we have verified that the median slit length is 7 arcsec, and that only few among the brightest objects suffer from this problem.

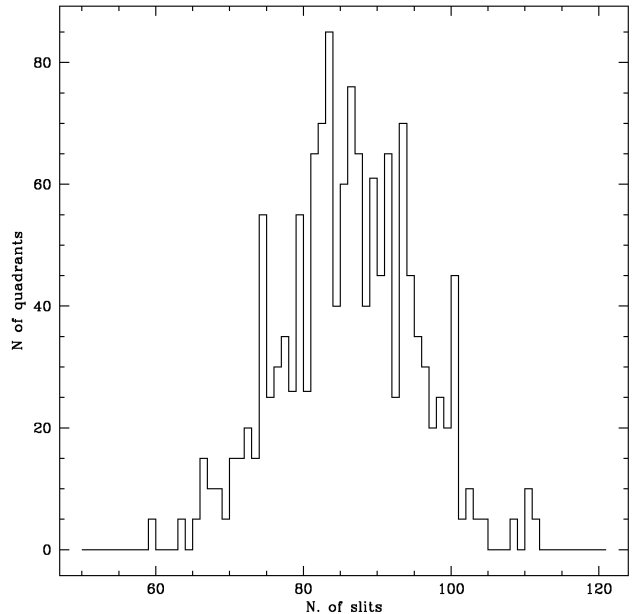


Fig. 2. The distribution of the number of slits per VIPERS quadrant.

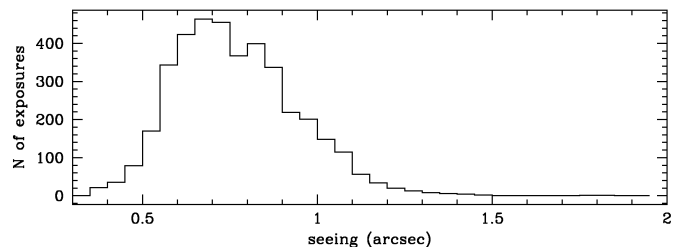


Fig. 3. The distribution of seeing values for VIPERS observations.

4. Spectroscopic observations and data reduction

4.1. Quality of VIMOS raw data

VIPERS observations started in September 2008 and have proceeded at a steady rate since then. The median airmass of PDR-1 data is 1.14, and remains below 1.3 in 90% of the exposures. To match the slit width and minimize slit losses, the requested maximum seeing was 1 arcsec. Figure 3 shows the seeing distribution as measured from the scientific exposures. The median seeing is 0.8 arcsec and 90% of exposures have a seeing below 1.05 arcsec. 85% of observations have been carried out in dark time, while the remaining fraction either had a moon illumination below 20%, or a moon distance above 70 deg.

In spring/summer 2010, VIMOS was upgraded with new red-sensitive CCDs in each of the 4 channels (Hammersley et al. 2010). The original thinned E2V detectors were replaced by twice-thicker E2V devices, considerably lowering the fringing and increasing the quantum efficiency by up to a factor two over the wavelength range of the LR-Red grism. The lesser (almost non-existent) fringing allows for a better sky subtraction redwards of 7500 \AA (where OH bands dominate the sky emission), which improves the data quality. In the following, we use the term ‘epoch 1’ to denote data acquired before the refurbishment, and ‘epoch 2’ for data acquired afterwards. In Figure 4 we



Fig. 4. A typical 2D extracted spectrum from epoch 1 data (top) and epoch 2 data (bottom). Wavelength ranges from 5600Å to 9500Å from left to right. Spatial direction is along the y axis.

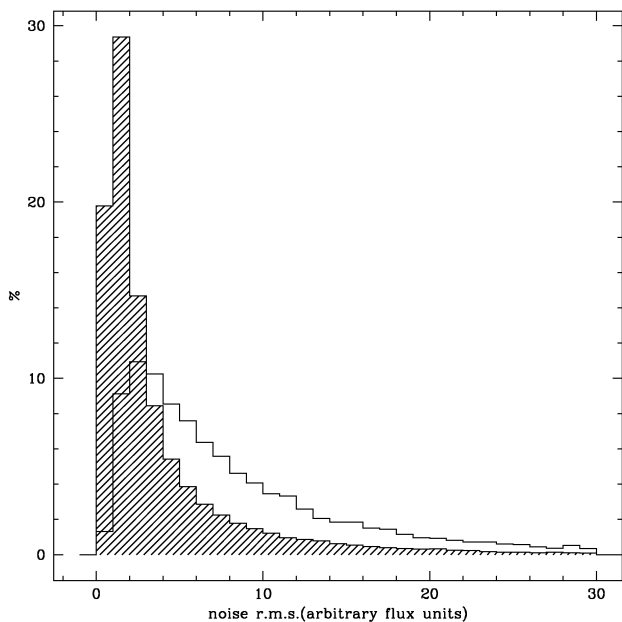


Fig. 5. Median noise r.m.s. distribution of the VIPERS spectra in the 7500-9100Å wavelength range. Empty histogram refers to data acquired before VIMOS refurbishment, shaded histogram to those acquired after the refurbishment.

show a typical 2D extracted spectrum from epoch 1 data (top) and epoch 2 data (bottom). The improved sky subtraction in epoch 2 data is clearly visible. More quantitatively, Figure 5 shows the distribution of the r.m.s. of the sky subtraction residuals in the 7500-9100Å wavelength range for epoch 1 (empty histogram) and epoch 2 (shaded histogram) data. The median of the distribution diminishes by a factor 2.6, clearly demonstrating the significant improvement in the sky subtraction. In Section 5 we will show how this affects the redshift measurement. The VIMOS upgrade also included substituting the old passive flexure compensation system with a new active flexure compensator (AFC), which should be more reliable and precise. Unfortunately, for a few months the AFC was operational only during target acquisition. In other words, some observing runs were actually carried out without any flexure compensation system during the spectroscopic exposure. This implies that during the same OB the images of the slits moved up to 2 pixels on the detector plane. To account for this effect, we have modified the reduction pipeline to perform the slit tracing exposure by exposure. Since the arc lamp is always acquired at the end of the OB, its tracing is slightly different from the tracing of the first expo-

sure, implying that the wavelength calibration at the slit edges is not as good as at the slit centre. This has a minor effect on the quality of the sky subtraction: unless the object is very far from the slit centre, the only consequence is that 2D spectra are noisier close to the edges. In Section 5 we will show that the redshift measurement is statistically unaffected.

4.2. Data reduction procedure

VIPERS data reduction is performed with a fully automated pipeline, starting from the raw data and flowing down to the wavelength- and flux-calibrated spectra and redshift measurement. The pipeline is an updated version of the algorithms and dataflow from the original VIPGI system, fully described in Scodreggio et al. (2005). We summarise here the main concepts.

As a first step, in each raw frame the 2D dispersed spectra are located and traced. Each raw spectrum is collapsed along the dispersion direction, and the object location computed. A first sky subtraction is performed row by row, avoiding the region identified as the object. An inverse dispersion solution is computed for each column of each dispersed spectrum making use of an arc calibration lamp. The wavelength calibration residuals distribution is well peaked around 0.771Å (i.e. 1/10 of a pixel) and 97% of spectra have a wavelength calibration uncertainty below 1.25Å (1/5 of a pixel). The inverse dispersion solution is applied before extraction. A further check on the wavelength of sky lines is computed on the linearized 2D spectra, and, if needed, a rigid offset applied to data in order to bring the sky lines to their correct wavelength. The different scientific exposures of the same field are registered and co-added, and a second background subtraction is performed repeating the procedure carried out before. Finally, 1D spectra are extracted applying the Horne extraction algorithm (Horne 1986), and spectra are corrected for the instrument sensitivity function, as derived from the standard spectrophotometric observations routinely carried out by ESO. Given a 2D spectrum, we can compute sky subtraction residuals as

$$\langle \text{skyResidual} \rangle_i = \frac{\sum_{j \in \text{NRegion}} (\langle C \rangle - C_j)^2}{\text{NRegion} - 1}, \quad (4)$$

where NRegion is the number of pixels in the sky region on one side of the object, $\langle C \rangle$ is the mean of the counts in the sky region and C_j are the counts in pixel j , at wavelength i . This computation is done on both sides of the object (resL and resR), taking into account slit borders and possible second objects in the slit. From such residuals, a mean noise spectrum is computed, the noise in the i -th pixel being given by

$$\text{noise}_i^2 = \frac{\text{resL}_i + \text{resR}_i}{2} + S_i = \langle \text{skyResidual} \rangle_i + S_i, \quad (5)$$

where S_i are the source counts at wavelength i . To obtain fully flux calibrated spectra, while correcting for slit losses, we have convolved each spectrum with the CFHTLS i filter response function, and computed a normalization factor between the spectrum and the photometric magnitude. We then run EZ (Garilli et al. 2010) on all 1D extracted spectra for a first automatic redshift measurement. All data reduction has been centralised in our data reduction and management centre at INAF – IASF Milano. When ready, the fully reduced data are made available to the team within a dedicated database. The full management of these operations within the *EasyLife* environment is described in Garilli et al. (2012).

4.3. Redshift estimation, reliability flags and confidence levels

In most cases, the final redshift measurement is performed and validated by two team members independently. The reliability of the measured redshifts is quantified at the time of validation following a scheme similar to that used for the VVDS (Le Fèvre et al. 2005) and zCosmos surveys (Lilly et al. 2007). Measurements of stars and galaxies are flagged using the following convention:

- Flag 4: a highly reliable redshift (estimated to have $> 95\%$ probability of being correct), based on a high SNR spectrum and supported by obvious and consistent spectral features.
- Flag 3: also a very reliable redshift, comparable in confidence with Flag 4, supported by clear spectral features in the spectrum, but not necessarily with high SNR.
- Flag 2: a fairly reliable redshift measurement, but not as straightforward to confirm as for Flags 3 and 4, supported by cross-correlation results, continuum shape and some spectral features, with expected chance of $\approx 75\%$ to be correct. We shall see in the following that the actual estimated confidence level will turn out to be significantly better.
- Flag 1: a reasonable redshift measurement, based on weak spectral features and/or continuum shape, for which there is roughly a 50% chance that the redshift is actually wrong.
- Flag 0: no reliable spectroscopic redshift measurement was possible.
- Flag 9: a redshift based on only one single clear spectral emission feature.
- Flag -10: spectrum with clear problems in the observation or data processing phases. It can be a failure in the *vmmips* Sky to CCD conversion (especially at field corners), or a failed extraction by VIPGI (Scodreggio et al. 2005), or a bad sky subtraction because the object is too close to the edge of the slit.

Broad-Line AGN can be easily identified during the validation process from the width of their emission lines. The flagging system for AGN is similar, though not identical, to the one adopted for stars and galaxies:

- Flag 14: secure AGN with a $> 95\%$ reliable redshift, including at least 2 broad lines;
- Flag 13: secure AGN with good confidence redshift, based on one broad line and some faint additional feature;
- Flag 19: secure AGN with one single secure emission line feature, redshift based on this line only;
- Flag 12: a $> 95\%$ reliable redshift measurement, but lines are not significantly broad, might not be an AGN;
- Flag 11: a tentative redshift measurement, with spectral features not significantly broad.

Serendipitous (also called secondary) objects appearing by chance within the slit of the main target are identified by adding a ‘2’ in front of the main flag. In Section 4.5 we will assess the actual confidence levels of the flags by comparing with results of other surveys.

Once the final review of the redshifts is complete, a decimal part of the flag ‘.X’ indicating concordance or discordance with the photometric redshift is added to the main flag. An automatic algorithm cross-correlates the spectroscopic measurement (z_{spec}) with the corresponding photometric redshift (z_{phot}), estimated from the five-band CFHTLS photometry using the *Le Phare* code (Ilbert et al. 2006; Arnouts & Ilbert 2011). The 68% confidence interval $[z_{\text{ph-min}}, z_{\text{ph-max}}]$ (in general not symmetric) based on the PDF of the estimated z_{phot} is provided by *Le Phare*. If z_{spec} is included within the $z_{\text{ph-min}} - z_{\text{ph-max}}$ range, spectroscopic and photometric redshifts are considered in agreement and a flag 0.5 is added to the primary flag. Redshifts are instead in marginal agreement (and a flag 0.4 is added) when they are comparable only at the 2σ level, where 2σ is the minimum (maximum) between $z_{\text{phot}} - 0.05 \times (1 + z_{\text{phot}})$ and $z_{\text{phot-min}}$ ($z_{\text{phot}} + 0.05 \times (1 + z_{\text{phot}})$ and $z_{\text{phot-max}}$), being 0.05 twice the median scatter of the comparison between z_{spec} and z_{phot} . This allows us to signal cases in which the PDF of the single measurement is rather narrow, but still the spectroscopic redshift is close. Finally, we add ‘0.2’ to the redshift flag when neither of the two criteria is satisfied, and ‘0.1’ when no z_{phot} estimate is available.

Thus, whatever the primary integer flag is, a flag ‘*.5’ or ‘*.4’ is an indication supporting the correctness of the redshift. This is particularly useful in the case of highly uncertain, flag = 1 objects, for which the confidence level can be increased by the agreement with the photometric redshift value. In all VIPERS papers redshifts with flags ranging between 2.X and 9.X are referred to as reliable redshifts and are the only ones normally used in the science analysis.

4.4. Repeated observations and redshift errors

The footprint of VIMOS is not a perfect rectangle, as each quadrant has a slightly different width. When designing the survey pointings, we have allowed for a small overlap (of the order of few arcseconds) between adjacent pointings. For this reason a number of VIPERS targets have been observed twice. Objects falling within this overlapping region have some chance of being observed twice, and this happened for 783 objects in the VIPERS survey. Additionally, during the re-commissioning of VIMOS after the CCD refurbishment in summer 2010, a few pointings were re-observed to verify the performance with the new setup (Hammersley et al. 2010), targeting further 1357 objects. In total, this results in a very useful sample of 2143 objects observed at least twice. After excluding second objects, stars and AGNs, we are left with 1235 target galaxies yielding a reliable redshift (i.e. with a flag ≥ 2) in both measurements, of which 1192 have compatible measurement, i.e. the two redshifts differ by less than $\Delta/(1+z) < 3\sigma_z \approx 0.0025$. This subsample can be used to obtain an estimate of the internal r.m.s. value of the redshift error of VIPERS galaxies, as discussed in Guzzo et al. (2013) and reported here for completeness. In Figure 6, top panel, we show the distribution of rest frame velocity difference for these compatible measurements. The distribution is well fitted by a Gaussian centred on the origin with a standard deviation of $\sigma = 200 \text{ km s}^{-1}$, corresponding to a single-object 1σ error $\sigma_v = \sigma_z/2^{1/2} = 141 \text{ km s}^{-1}$. In terms of redshift, this yields a standard deviation on the redshift measurements

Table 2. Confidence of redshift flags

VIPERS Class (Flags)	Comparison Class (Flags)	N. of Common Galaxies	Concordant Redshifts	VIPERS Confidence Level
VIPERS Internal				
3,4	3,4	654	648	99.5%
2,9	3,4	385	373	98.4%
2	2	151	129	92.4%
VIPERS vs. VVDS				
3,4	3,4	346	336	98.5%
2,9	3,4	74	66	90.6%
VIPERS vs. PRIMUS				
3,4	3,4	1619	1478	95.5%
2,9	3,4	876	708	84.6%

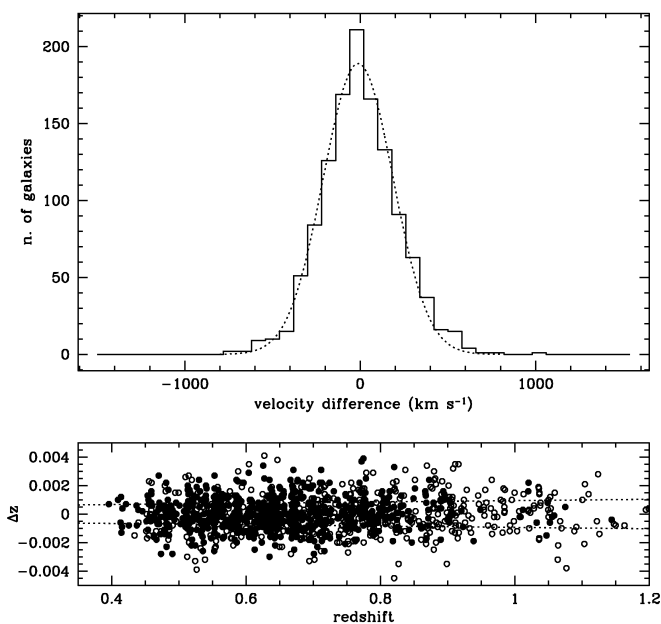


Fig. 6. The distribution of the differences between two independent redshift measurements of the same object, obtained from a set of 1192 VIPERS galaxies with redshift flag ≥ 2 . Top: distribution of the velocity differences $\Delta v = c\Delta z/(1+z)$. Catastrophic failures, defined as being discrepant by more than $\Delta z = 6.6 \times 10^{-3}(1+z)$, have been excluded. The best-fitting Gaussian has a dispersion of $\sigma_2 = 200 \text{ km s}^{-1}$, corresponding to a single-object *rms* error $\sigma_v = \sigma_2/\sqrt{2} = 141 \text{ km s}^{-1}$. In terms of redshift, this translates into a standard deviation of $\sigma_z = 0.00047(1+z)$ for a single galaxy measurement. In the bottom panel, the darker dots correspond to highly reliable redshifts (i.e. flags 3 and 4), which show a dispersion substantially similar to the complete sample (see text).

of $0.00047(1+z)$. Using only the most reliable spectra (i.e. flags 3 or 4 in both measurements), we are left with 648 double measurements and the resulting rest-frame 2-object dispersion decreases to $\sigma_2 = 195 \text{ km s}^{-1}$. This indicates that flags 9, 2, 3 and 4 are substantially equivalent in terms of redshift precision.

4.5. Statistical confidence levels corresponding to redshift flags

A first estimate of the actual, statistical confidence level of the redshift flags associated to our redshift measurements has been presented in Guzzo et al. (2013) using the available duplicated observations mentioned above. These results are reported in the top part of Table 2. Here we extend and complement this analysis, making use of external measurements.

The confidence level of a given Flag class (e.g. Flag 3+4) from VIPERS, which we call survey X for simplicity, can be estimated from the fraction of measurements in agreement among those galaxies observed independently by another survey, Y , with comparable or better reliability. We note that while this latter aspect is easy to evaluate when comparing VIPERS to a survey like VVDS, which was observed with a very similar set-up, evaluating the intrinsic redshift reliability of a very different data set, for which additionally we may only have literature information, is less straightforward. This will be the case for the second comparison case discussed below, i.e. the PRIMUS survey.

In practice, if N_{meas} is the number of common measurements and N_{agree} is the number of redshifts in agreement², then the probability for two redshifts to agree corresponds to the combined probability that X and Y give the correct redshift, i.e.

$$P(X|Y) = \frac{P(X) \times P(Y) = N_{\text{agree}}}{N_{\text{meas}}} \quad (6)$$

If we are considering the same Flag category for both data sets and assume that the flags indicate similar confidence levels for the measurements, then $P(X) \simeq P(Y)$ and thus

$$P(X) = \sqrt{\frac{N_{\text{agree}}}{N_{\text{meas}}}} \quad (7)$$

If on the other hand we are comparing two classes with different intrinsic confidence levels, we need to estimate that of the reference class (e.g. $P(Y)$), to be able to compute $P(X)$, i.e.

$$P(X) = \frac{1}{P(Y)} \frac{N_{\text{agree}}}{N_{\text{meas}}} \quad (8)$$

While for internal data it is often straightforward to estimate $P(Y)$, this is non-trivial for data obtained from the literature, unless it is certain that the reference class is of much higher reliability than the one for which we want to estimate the confidence. In such a case, $P(Y) \simeq 1$ can be a reasonable assumption.

² As above, two redshift measurements are defined to be ‘in agreement’ when their difference $\Delta/(1+z) < 3\sigma_z \simeq 0.0025$.

Comparison to VVDS. Some areas within both W1 and W4 fields have been observed within the VVDS survey and a similar comparison between VIPERS and VVDS has been presented in Le Fèvre et al. (2013). Let us make the reasonable assumption that the typical redshift error in VVDS and VIPERS are comparable, with rms dispersion σ_z . We are aware that an improvement in SNR has certainly been introduced for the VIPERS data by the refurbishment of the detectors in 2010; our assumption will only make the comparison more conservative for VIPERS. There are 420 objects with a reliable (flag 2 through 9) redshift in VIPERS which have a highly reliable (flag 3 and 4) in VVDS.

The results are shown in the central part of Table 2. We first compared VIPERS Flag 3 and 4 redshifts with the same class of VVDS, obtaining a confidence level of 98.5%; this is very consistent with the value 99.6% estimated internally using VIPERS repeated observations. For the flags 2 and 9 together we instead obtain a confidence level of 90.6%, against the higher confidence, 98.4%, estimated from the repeated VIPERS observations.

Comparison to PRIMUS. W1 is also one of the areas selected by the PRIMUS survey (Cool et al. 2013). Using only the PRIMUS reliable objects (PRIMUS flag 3 and 4), there are 2495 objects for which VIPERS measures a reliable redshift (flag 2 through 9) in VIPERS. For this comparison, we consider two measurements to be concordant when $\Delta/(1+z) < 3(\sigma_{z\text{VIPERS}}^2 + \sigma_{z\text{PRIMUS}}^2)^{1/2}$, where $\sigma_{z\text{PRIMUS}} = 0.003$ for PRIMUS flag=4 and $\sigma_{z\text{PRIMUS}} = 0.015$ for PRIMUS flag=3 (Cool et al. 2013)

The results are shown in the bottom part of Table 2. Both redshift classes considered (Flags 3+4 and 2+9) give slightly smaller confidence level, when compared to PRIMUS. The problem in interpreting these results is whether the confidence levels corresponding to the PRIMUS flag system are similar to those of VIPERS or VVDS. We note that PRIMUS spectra have a coarser resolution than VIPERS ones, with R degrading from 100 to 20 from blue to red. Taking this into account, the agreement of the Flag 3+4 classes for the two data sets is very good. In particular, the difference in the results in the first lines (Flags 3,4 vs 3,4) for the ‘VIPERS Internal’ and ‘VIPERS vs. PRIMUS’ cases in the Table is probably more a test for the PRIMUS best redshifts, rather than for VIPERS.

Overall, the consistency of the estimates performed internally (top) and with VVDS (middle), indicates that redshifts for Flags 3+4 in VIPERS should have a 99% confidence of being correct, while class 2+9 is expected to have a confidence level of at least 90%, probably close to 95%. If we compare these confidence levels to those indicated in the original prescriptions for the flag assignments, summarized in § 4.3, we see that in particular for the Flag 2 objects the actual redshifts are more reliable than expected.

5. The VIPERS PDR-1 sample

We define the observed target sampling rate as the ratio between the observed target objects and all possible targets within the spectroscopic area. The detection rate is the percentage of detected targets over observed targets, while the redshift measurement success rate and reliable measurement success rate are the fraction of measured and reliably measured objects over the detected ones. The X-ray AGN candidates are excluded from this computation, as they are put in masks as compulsory objects (see Section 2.2), and as such follow a different selection function. In Table 3 we show some basic statistics of the VIPERS PDR-

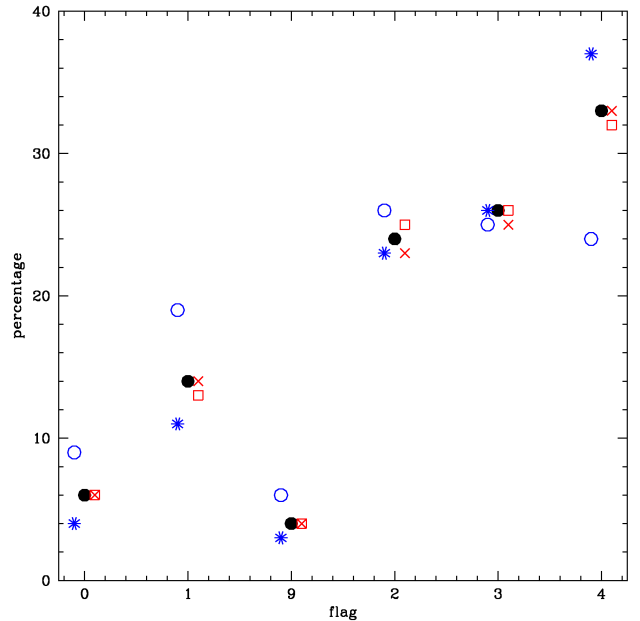


Fig. 7. Fraction of redshift flags as from Table 4: filled points for the full sample, open red squares for the W1 sample, red crosses for the W4 sample, blue open circles and stars for epoch1 and epoch2 samples respectively. W1 and W4 points as well as epoch1 and epoch2 points have been shifted along the x axis for clarity.

1 spectroscopic sample, split for W1 and W4, and for epoch 1 and epoch 2 data. Numbers in parenthesis indicate the fractions of the different spectroscopic flags. So far, we have observed 63 942 objects (62 862 targets plus 1080 serendipitous objects) with a detection rate of 96%. The detection rate shows no difference between W1 and W4, nor between epoch 1 and epoch 2 data (see section 3). Table 3 reveals the excellent quality of VIPERS spectroscopic data: globally the redshift measurement success rate is 94%. 81% of the objects have a reliable redshift, with 58% of the redshift with a confidence level higher than 99% (flag 3 and 4). In the last two rows in Table 3 we show the detection rate and redshift measurement rate split into epoch2a, when no flexure compensation was active during exposures, and epoch2b, when the active flexure compensator was working correctly. The identical detection and measurement rates demonstrate that our reduction pipeline has successfully recovered for this effect.

Table 4 and Figure 7 show the percentage of the various redshift flags. For the purpose of this table and figure, the distinction between AGN and galaxies/stars has been neglected so that flags 1.x include also flags 11.x, flags 2.x include flags 12.x, and so on. The better quality of epoch 2 data is clearly demonstrated by the much lower fraction of flags 0 (which decreases from 9% to 4 and 1 (decreasing from 19% to 11%), and the much higher fraction of flags 4 (rising from 24% to 37%).

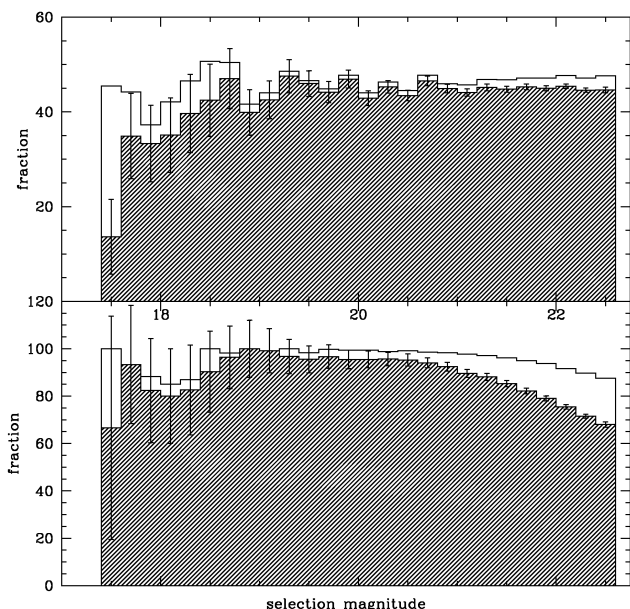
Figure 8 shows the overall sampling of the VIPERS survey as a function of magnitude. The observed target sampling rate (top panel, empty histogram) is remarkably stable, demonstrating that our target selection criterion is not flux dependent. Fainter than i_{AB} the detection rate (top panel, shaded histogram) is constant around 45%. The slight decrease we observe at brighter magnitudes is probably due to the short slits affecting the extraction of the brighter objects. We emphasise that such a decrease remains within the uncertainties but for the very first magnitude bin and we are currently revising the spectra ex-

Table 3. VIPERS detection rate. Numbers in parenthesis indicate the fraction over the observed targets (column 2) and detected targets (columns 3 and 4).

Field	Observed targets	Detected targets	Measured redshifts	Reliable redshifts
W1	31602	30244 (96%)	28376 (94%)	24553 (81%)
W4	31260	29897 (96%)	28041 (94%)	24050 (80%)
epoch 1	22049	21212 (96%)	19209 (91%)	15541 (73%)
epoch 2	40813	38929 (95%)	37208 (96%)	33062 (85%)
epoch 2a	10236	9813 (96%)	9464 (96%)	8495 (87%)
epoch 2b	30577	29116 (95%)	27744 (95%)	24567 (84%)
total	62862	60141 (96%)	56417 (94%)	48603 (81%)

Table 4. VIPERS redshift flag distribution. Numbers in parenthesis indicate the fraction of the different spectroscopic flags over detected targets.

Field	Flag 0.x	Flag 1.x	flag 9.x	flag 2.x	flag 3.x	flag 4.x
W1	1863 (6%)	3823 (13%)	1132 (4%)	7081 (25%)	7283 (26%)	9057 (32%)
W4	1825 (6%)	3991 (14%)	1109 (4%)	6519 (23%)	7112 (25%)	9310 (33%)
epoch 1	1983 (9%)	3668 (19%)	1091 (6%)	5086 (26%)	4785 (25%)	4579 (24%)
epoch 2	1705 (4%)	4146 (11%)	1150 (3%)	8514 (23%)	9610 (26%)	13788 (37%)
total	3688 (6%)	7814 (14%)	2241 (4%)	13600 (24%)	14395 (26%)	18367 (33%)


Fig. 8. Top: observed target sampling rate (empty histogram), and detection rate (shaded histogram) for the VIPERS survey targets. Bottom: redshift measurement success rate (empty histogram), and reliable measurement success rate (shaded histogram) targets. Error bars are indicated for shaded histogram only for clarity.

traction procedure to ameliorate this effect. Conversely, there is a clear (albeit small) trend for redshift measurement success rate to diminish with increasing object flux (bottom panel, empty histogram): in the last half-magnitude bin the fraction of objects for which a redshift measurement is available drops from 93% to 88%. This drop becomes even more dramatic when only reliable measurements are considered (bottom panel, shaded histogram). In section 6 we will illustrate how it is possible to account for these effects statistically when using the VIPERS spectroscopic sample.

Table 5. VIPERS measured redshift for stars galaxies and AGN

Field	galaxies	reliable galaxies	stars	AGN	reliable AGN
W1	27336	23662	598	442	380
W4	26010	22196	1648	383	338
second objects	581	371	202	4	3
total	53927	46229	2448	829	721

5.1. Redshift distribution

Table 5 shows the number of target and serendipitous stars, galaxies and AGN, considering all measurements or only reliable (flags 9.x, 2.x, 3.x, 4.x) redshifts. The stellar contamination is impressively low ($\sim 4\%$), demonstrating that the adopted criterion for excluding stars from the sample works well. The higher number of stars in the W4 area reflects the lower galactic latitude of this field with respect to W1 (-44 degrees and -57 degrees respectively). Figure 9 shows the redshift distribution for the whole VIPERS sample (top panel), the galaxy sample (middle panel) and the AGN sample (bottom panel). The observed redshift distribution shows that our selection criterion works well in excluding low redshift galaxies. As expected, the highest redshift tail is made up of AGN, while only a handful of galaxies have a redshift above 1.5.

6. Survey selection function: masks and weights

The survey selection function quantifies the actual probability that a galaxy with given properties at a given position on the sky is actually observed by VIPERS. This can be a binary probability, as implied by the global survey geometry and instrumental footprint, or a more complex function of position on the sky (as e.g. introduced by a varying sampling rate due to the limited number of slits that can be accommodated in each quadrant). In more detail, it can include a continuous function that depends in general on the galaxy flux, colour, spectral properties and redshift. The accurate knowledge of the actual selection function resulting from all these effects allows us to define a set of weights to be applied to each galaxy. These are

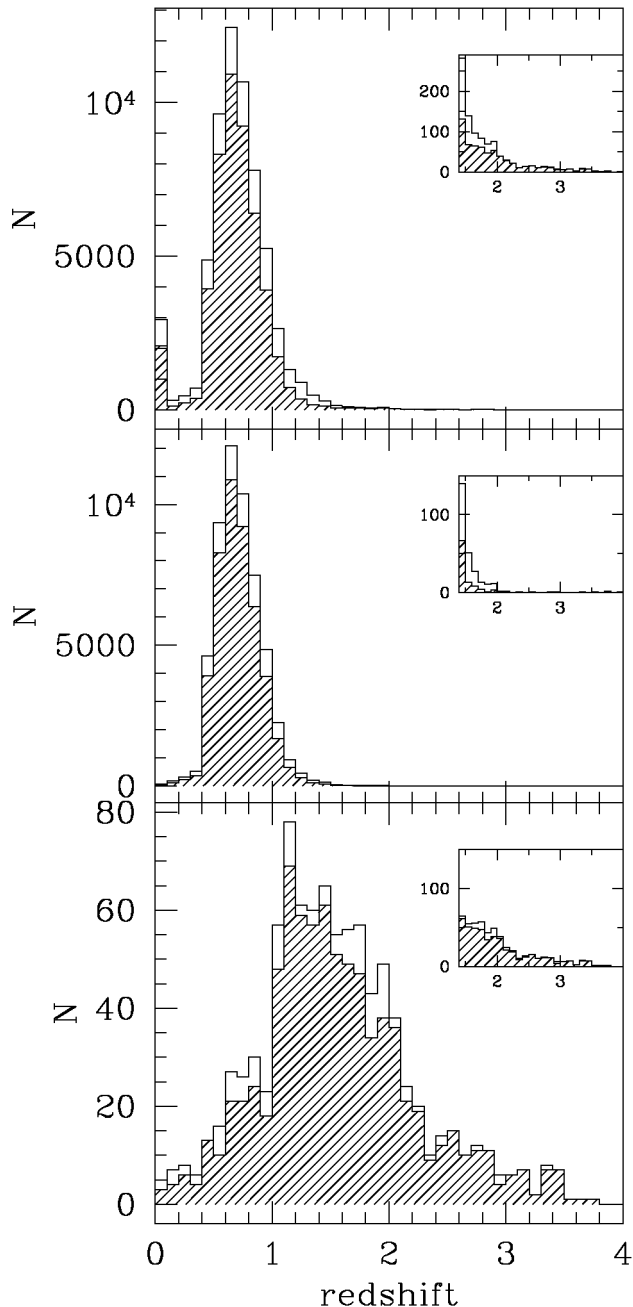


Fig. 9. Redshift distribution for the VIPERS survey Top: all objects, middle: only galaxies; bottom: only AGN. The smaller insets zoom on the high redshift tail. The histograms include secondary objects. Empty histograms are for all measured objects, shaded histogram for reliably measured redshifts.

used to renormalize the observed density and two-point statistics to those one would ideally obtain from a statistically complete sample. In this section we shall describe in some detail how the different contributions have been estimated and encapsulated into a set of masks and weights describing the VIPERS selection function, which are provided to the general user together with the data release. These same masks and weights have been used, for example, in the estimate of the VIPERS mass and luminosity functions (Davidzon et al. 2013; Fritz et al. 2013) and in the clustering studies of de la Torre et al. (2013) and Marulli et al.

(2013), where further details can be found.

6.1. Photometric and Spectroscopic Masks

First, we consider selection effects arising from the CFHTLS parent catalogue. The photometric survey is not free from defects and there exist a small number of gaps due to failed observations and artefacts associated with bright stars that affect the VIPERS area. These regions are treated as holes in the survey and are described by a photometric mask.

The area surveyed by the spectroscopic observations may be described by the geometry of the VIMOS footprint and the layout of the observed pointings. Although the instrument geometry is fixed from night to night, particular observing conditions can modify the effective area. For instance, in certain observing configurations, a VIMOS quadrant may be partially obscured by the telescope guider arm. We have reconstructed the precise geometry of each quadrant and recorded it as a polygon. The combination of such polygons defines a second binary mask, which allows a precise reconstruction of the overall survey footprint on the sky. The construction of the photometric and survey masks is described in detail in Guzzo et al. (2013).

The application of the two masks to the whole target catalogue (see Section 2) defines what in the following we call the parent sample.

6.2. Target Sampling Rate

Only $\approx 45\%$ of the available targets in the parent sample may be assigned a slit and observed according to the slit-assignment strategy. The galaxy Target Sampling Rate (TSR) is defined as the fraction of candidate galaxies (according to our selection criterion, see Section 2) in the parent sample for which a spectrum has been acquired. Note that this is slightly different from the target detection rate shown in Figure 8 and Table 3, where also AGN candidates were considered. The TSR is both a function of angular position on the sky and apparent flux.

As for all multi-object spectrographs, the TSR varies with location on the sky, depending on the fluctuations in the surface density of objects. In particular, the single pass strategy of VIPERS generates a *proximity bias*, in which galaxy close pairs are disfavoured. This is particularly relevant in two-point statistical studies, e.g. for two-point correlation functions, for which a specific correction based on the angular clustering of the measured and parent samples has to be applied (de la Torre et al. 2013). The TSR as defined here (indicated as $\text{TSR}(Q)$ in the following) maps the quadrant to quadrant variations in the target sampling.

Given the way we have built the spectroscopic masks (see section 2), the TSR is expected to be independent of the target apparent selection magnitude. Still, a very slight magnitude dependence exists at very bright magnitudes (see Figure 8, top panel). This can be due either to the higher angular clustering of the brightest objects, or to the short slits which may disfavour the very largest objects (see Section 3), or to a combination of both effects. The TSR used in published papers (and distributed as part of this release) takes this effect into account: see Davidzon et al. (2013); Fritz et al. (2013) for details.

6.3. Spectroscopic Success Rate

The Spectroscopic Success Rate (SSR) is defined as the fraction of measured candidate galaxy targets with a reliable (flag 2,3,4,9) galaxy redshift measurement over all the detected galaxy targets. As for the TSR, this is slightly different from the reliable measurements success rate shown in Figure 8 and Table 3, where we have included also AGN candidates. The SSR is clearly sensitive to both the observing conditions and the apparent magnitude. A second order dependence on spectral type and redshift is usually present, as, at a given magnitude, it can be easier to measure redshifts for strong emission line galaxies, if the emission lines fall within the observed wavelength range.

In the clustering analysis of de la Torre et al. (2013), the angular dependence of the SSR (SSR(Q)) was estimated as a function of VIMOS quadrant as the ratio between the number of reliable redshift (flag 2.* $\leq z_{\text{flag}} \leq 9$.) and the total number of measured targets. The average SSR(Q) value is typically $> 80\%$, falling to 50% for quadrants observed in particularly poor conditions.

Note that, in principle, one can expect angular variations of the TSR and SSR on scales smaller than those of a single quadrant, for example due to the proximity bias discussed in the previous section or to an imperfect centring of the objects in the slit due to optical distortions. These effects cannot be viewed purely as a position-dependent probability of obtaining a redshift. This means that for some specific analyses, a more sophisticated treatment of these effects may be required, as discussed in de la Torre et al. (2013). The various information we provide within PDR-1 should in general allow such higher level of refinement, if required.

In the case of statistical analyses which are not sensitive to the angular position of objects, it is possible to disentangle the dependence of SSR on apparent magnitude and redshift using the full VIPERS sample and use only the SSR(mag, z) completeness weights (Davidzon et al. 2013; Fritz et al. 2013). The SSR(mag, z) has been estimated by computing the ratio of the number of successful galaxy redshift to the total number of detected galaxy targets per magnitude and redshift bins. However, it is important to note that the SSR(mag, z) corresponds to the SSR averaged over all quadrants and cannot be used simultaneously with the SSR(Q) previously defined, which instead corresponds to the averaged SSR over the magnitude and redshift distributions in a given quadrant.

6.4. Colour Sampling Rate

The Colour Sampling Rate (CSR) defines the completeness of galaxies detected in spectroscopy with respect to a purely $i' < 22.5$ magnitude-limited sample. It accounts for the missed galaxies at the boundaries of the colour-based redshift selection criterion. Such incompleteness affects only galaxies with redshift close to the nominal lower limit of $z \approx 0.5$. The adopted colour criteria were in fact calibrated using the purely flux limited data of the VVDS survey (Guzzo et al. 2013). These calibration tests show that in the $(r - i)$ vs $(u - g)$ plane, the distance of a galaxy from the adopted threshold is a monotonic function of redshift. As such, the CSR is expected to be close to a step function changing from 0 to 1 around the nominal redshift threshold of $z = 0.5$.

To compute the CSR, we have used the VVDS Deep and Wide datasets, which not only are purely flux limited surveys but also share the same CFHTLS photometry of VIPERS. The result is shown in Figure 10. The measured CSR points are well

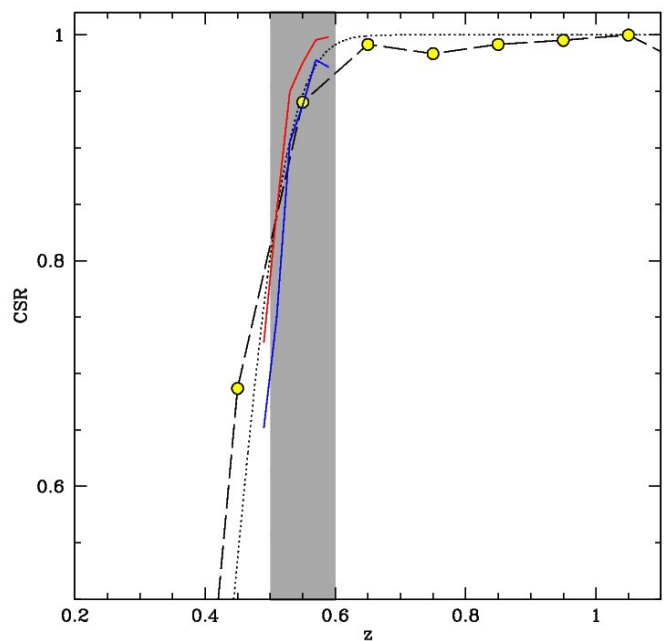


Fig. 10. Colour Sampling Rate (CSR) for the VIPERS spectroscopic sample. Dashed line and dots: the CSR as computed from the VVDS sample; dotted line: the functional fit; solid lines: CSR computed from the photometric sample for blue and red galaxies. The shaded area underlines the redshift range where the CSR has to be applied.

described by

$$\text{CSR}(z) = 0.5 - 0.5 \operatorname{erf}[b(z_t - z)], \quad (9)$$

where erf is the error function, $b = 10.8$ and $z_t = 0.44$. Compared to the VVDS data points, this fitting function only slightly overestimates the CSR (and therefore underestimates the weight) for galaxies at redshift $z = [0.55, 0.6]$. Comparison of the CSR obtained in this way to that obtained using photometric redshifts (therefore using a much larger number of galaxies), shows a very good agreement, as visible in Figure 10. We also checked whether passive and active galaxies show a different CSR, by splitting the sample on the basis of either the $NUVrK$ diagram or the $U - B$ bimodality (Fritz et al. 2013). As no significant difference has been found, we concluded that the only relevant dependence of the CSR is the one on redshift.

The final weight to be assigned to a given galaxy will be the product of the three weights mentioned above, i.e.

$$w = \text{TSR}^{-1} \cdot \text{SSR}^{-1} \cdot \text{CSR}^{-1} = w_{\text{TSR}} \cdot w_{\text{SSR}} \cdot w_{\text{CSR}}$$

In the case of angular position-dependent statistics, such as the two-point correlation function, the primary weights to be used are the TSR(Q) and SSR(Q) and the other dependences and possible corrections have to be studied in more details on a case-by-case basis (see de la Torre et al. (2013)).

7. VIPERS spectra

Figure 11 shows a few examples of VIPERS spectra, for galaxies with different redshift and reliability flag. All spectra have been normalized to the object i_{AB} magnitude (see Section 4).

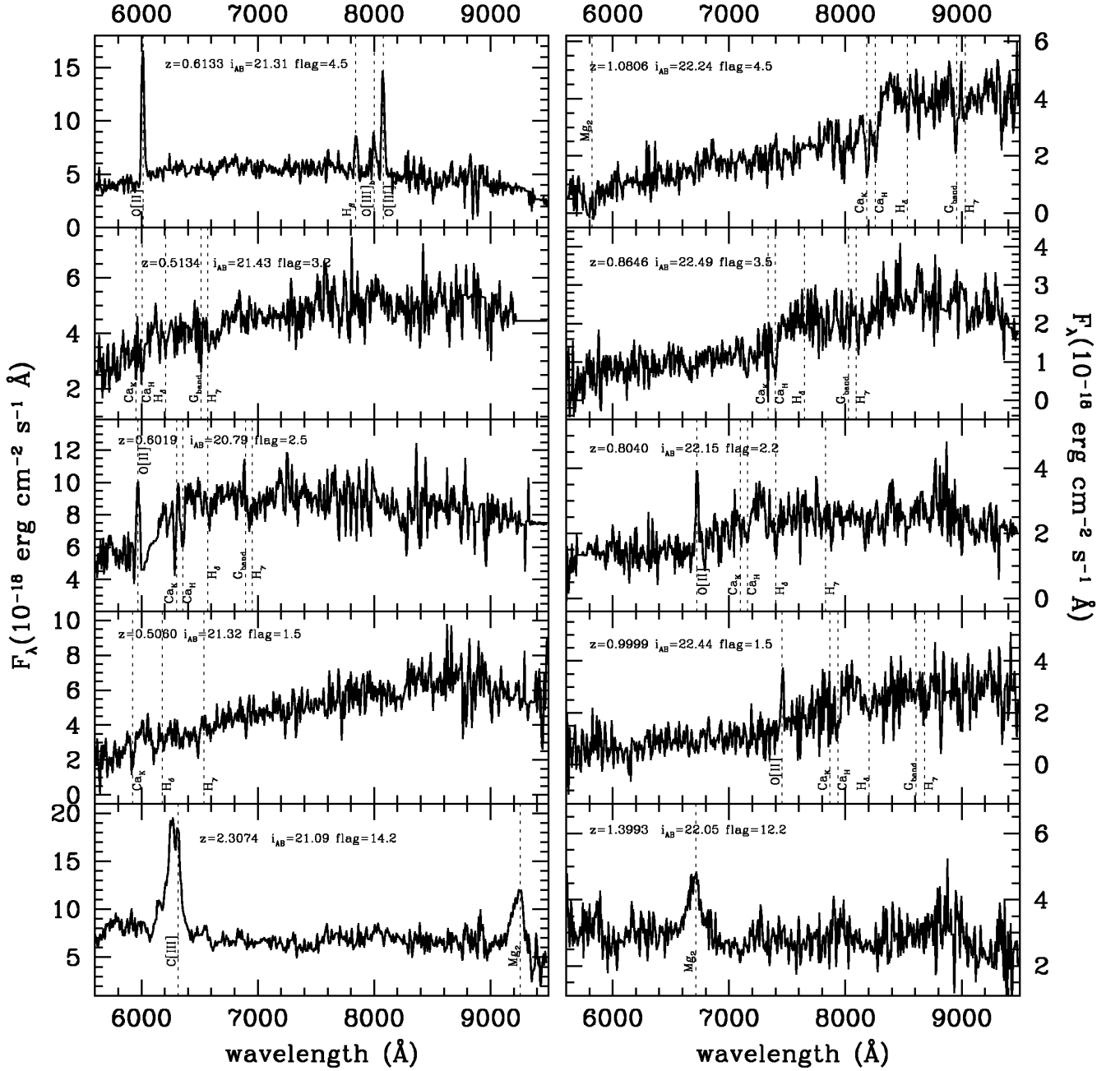


Fig. 11. Some representative VIPERS spectra: first column for mid-brightness objects, right column for objects close to the survey magnitude limit ($i_{AB} = 22.5$). Redshift reliability flags range from highest reliable (flag 4.5, first row) to least reliable (flag 1.5, 4th row). In the last row we show two AGN spectra.

7.1. Spectral feature measurements

Given the redshift distribution and the wavelength coverage of the VIPERS survey, the strongest spectral features which can be measured are the Balmer break and the most prominent emission lines, namely [OII], [OIII] doublet, [H β] and [H α]. The Balmer break ($D4000_n$) has been computed as the ratio between the mean flux measured over the 4000-4100 \AA range and the 3850-3950 \AA range (Balogh et al. 1999). The error on the $D4000_n$ break is computed by propagating the error on the two means. Measurement of line fluxes can be performed in various ways:

from the simplest pure flux integration below the line, to the most sophisticated approaches, which attempt to take into account the absorption component of the Balmer lines. The latter approach is particularly indicated when the purpose is to derive a precise estimate of the gas component, for example in all studies involving metallicity measurements. Our first aim is to separate emission line galaxies from non emission line galaxies, and for this reason we have chosen the simplest approach of pure flux integration below the line. All computations are done in counts and converted into fluxes using the counts-to-flux conversion factor derived from the instrument sensitivity function. For each line,

Table 6. Spectral feature parameters.

Spectral feature	Line Range	Continuum Range (blue)	Continuum Range (red)
[OII]	3710-3745	3600-3700	3755-4000
[OIII] _a	4990-5025	4700-4825	5035-5150
[OIII] _b	4900-4990	4700-4825	5035-5150
H _β	4845-4880	4700-4825	5035-5150
H _α	6535-6600	6350-6500	6610-6680

a local continuum per pixel unit is computed as the mean of the counts in two regions redwards and bluewards of the line :

$$C_{pix} = \frac{\sum_{i \in N_{contPix}} (C_i)}{N_{contPix}}. \quad (10)$$

where C_i are the counts in pixel i and $N_{contPix}$ are the pixels within the blue and red wavelength ranges used for the continuum computation. The error on the continuum level is computed using the noise spectrum associated to each source (see equation 5):

$$\sigma_{C_{pix}} = \frac{\sqrt{s^2 + < skyResidual >^2}}{\sqrt{N_{contPix}}}, \quad (11)$$

where s^2 is the continuum variance. The line counts are obtained integrating the continuum-subtracted counts in the defined line region

$$LineCounts = \sum_{i \in lineRegion} (C_i - C_{pix}) \quad (12)$$

and their error

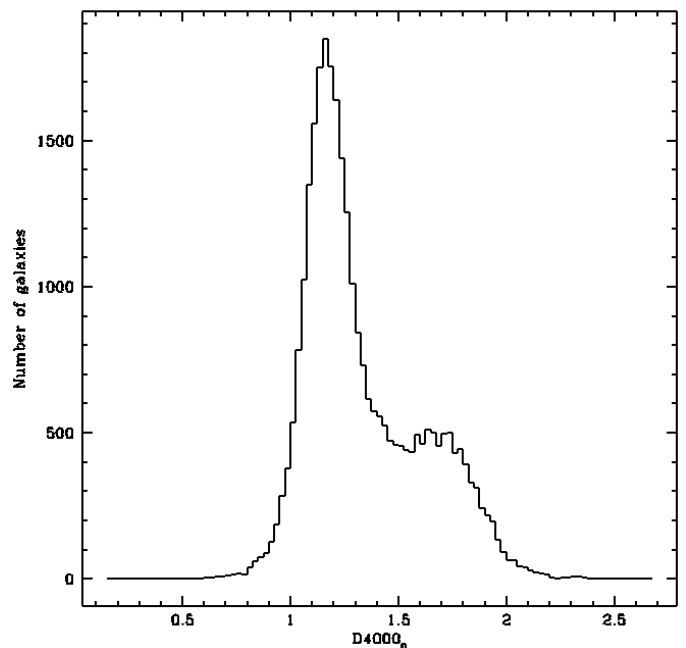
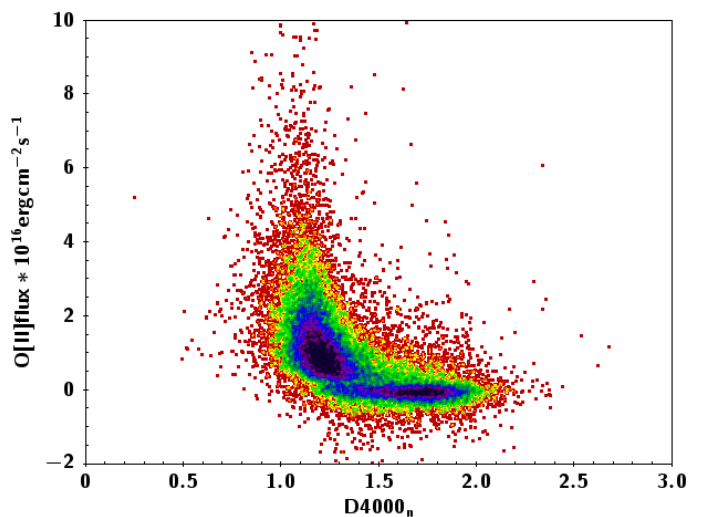
$$\sigma_{LC} = \sqrt{\sum_{i \in lineRegion} C_i + NL^2 * \sigma_{C_{pix}}^2} \quad (13)$$

where NL are the pixels within the line region. Table 6 gives the line and continuum boundaries we have used for the different features we have measured.

7.2. Spectroscopic properties

Spectroscopic information can be used to subdivide galaxies into different classes. In Figure 12 we show the distribution of the $D4000_n$ break amplitude for the subsample of flag 3 and 4 galaxies: its bimodality is evident. This figure is qualitatively identical to the bimodality plots presented in Fritz et al. (2013), which are based on the galaxy rest-frame $U - V$ colour. In Figure 13 we plot the [OII] flux as a function of the $D4000_n$ break value for the same galaxy subset. Negative values of the [OII] flux indicate a non detection of the line. In this Figure, the division into two large groups of galaxies is even more evident: most of the galaxies with a $D4000_n$ break larger than 1.5 have no or little sign of emission lines (or on-going star formation), while galaxies with strong on-going star formation are younger (i.e. have a lower $D4000_n$ break). A deeper classification of galaxies on the basis of spectral properties will be the subject of future work; here we restrict ourselves to investigating how the spectral features listed in Table 6 relate to other classification schemes used within the VIPERS project.

In Davidzon et al. (2013) an SED-based classification was proposed: according to the best fitting template, galaxies were


Fig. 12. Balmer break distribution for the subsample of flag 3 and 4 VIPERS galaxies.

Fig. 13. [OII] line flux vs. Balmer break amplitude density plot for the subsample of flag 3 and 4 VIPERS galaxies. Colour coding ranges from black to red with decreasing density.

divided into four SED types, where type 1 are red, old and supposedly quiescent galaxies, while type 4 are the bluest and most active galaxies. In Fritz et al. (2013) it is shown how, using this classification, type 1 galaxies define fairly well the red sequence in the colour magnitude diagram. We would expect type 1 galaxies to show no (or very little) sign of star formation activity. Figure 14 shows how the different SED type galaxies cluster in the $D4000_n$ -[OII] flux plane. Although on average type 1 galaxies show no sign of star formation, for 30% of them we detect significant (at least 3σ) [OII] emission. Conversely, type 4 galaxies totally dominate the high [OII] flux tail, and never show a prominent Balmer break. In other words, the SED based classification is rather efficient in isolating highly star forming galaxies (type 4), but the earlier type galaxies thus selected are not necessarily quiescent.

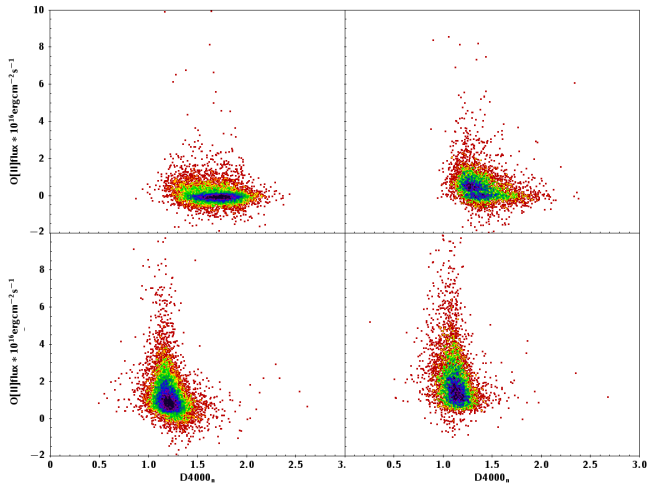


Fig. 14. [OII] line flux vs. Balmer break amplitude for the subsample of flag 3 and 4 VIPERS galaxies by SED type: type 1, top left; type 2, top right, type 3 bottom left, type 4 bottom right. Colour coding as in figure 13

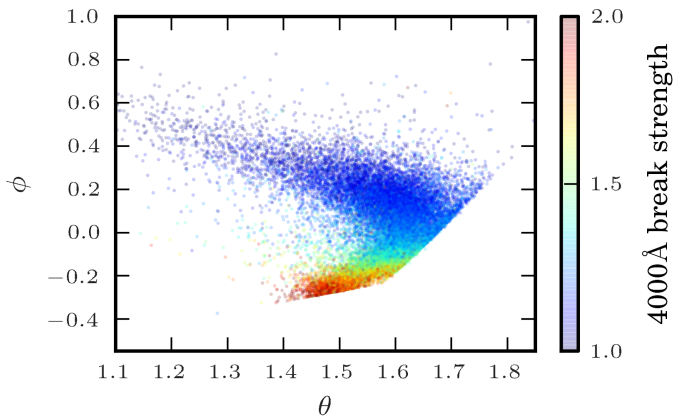


Fig. 15. The PCA galaxy classification plane, with Balmer break amplitude shown in colours.

A different approach was taken in Marchetti et al. (2013), where a Principal Component Analysis has been used to derive the first three eigen-coefficients, and a group-finding algorithm has been applied on the resulting θ - ϕ diagram, dividing galaxies into 15 different groups: groups from 1 to 8 comprise the classical types from E to Sc, while group from 9 to 15 comprise the more active StarBurst galaxies. In Figure 15 we show the PCA θ - ϕ diagram with galaxies in different colours according to their value of Balmer break. We can see that for galaxies showing $D4000_n$ higher than 1.5, the break amplitude is well correlated with the ϕ parameter. This is consistent to the classification proposed in Marchetti et al. (2013), who indicate this part of the diagram as being populated by the earlier galaxy types. Figure 16 relates the PCA θ - ϕ parameters with the flux of the [OII] emission line. The strongest emission line galaxies populate the locus of the StarBurst galaxies, as identified by the PCA classification. Galaxies in the locus of mid and late spirals ($\theta > 1.6$ and $\phi > 0$) do not seem to be strong [OII] emitters. This could partly be due to the limit on [OII] flux detection, and a more accurate analysis taking into account line detection upper limits will be done. Overall, there is a good agreement between the PCA based classification and the measured spectral features in identi-

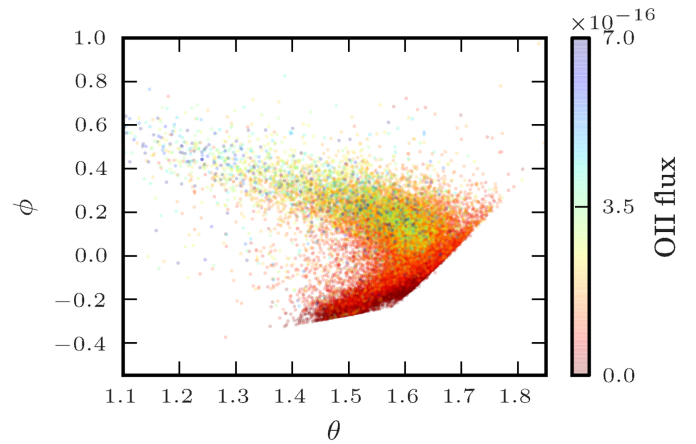


Fig. 16. The PCA galaxy classification plane, with [OII] line flux shown in colours.

Table 7. Spectral feature parameters

Group name	$D4000_n$ Range	Line Flux ¹ Range	N. of galaxies
G1	>1.7	undetected	3457
G2	1.55-1.7	undetected	1882
G3	>1.7	$> 3.0 \times 10^{-17}$	1135
G4	1.15-1.55	undetected	2539
G5	1.55-1.7	$> 3.0 \times 10^{-17}$	963
G6	1.15-1.55	$< 1.0 \times 10^{-16}$	6198
G7	<1.15	$< 1.0 \times 10^{-16}$	1123
G8	1.15-1.55	$> 1.0 \times 10^{-16}$	6681
G9	<1.15	$> 1.0 \times 10^{-16}$	4817

¹erg cm⁻²s⁻¹

fying the extreme galaxies (early types or Starbursts). This is not surprising, as PCA itself is based on spectral decomposition, and confirms the validity of the PCA approach.

7.3. Global spectral properties

The VIPERS spectral resolution $R \sim 250$ allows us to study individual spectroscopic properties only for galaxies with the highest signal to noise ratio. On the other hand, the high statistics provided by the VIPERS galaxy sample allows to define different galaxy groups (according to the scientific problem one may want to address), make high quality stacked spectra for each group and perform spectral measurement which would be impossible on the single objects. As an example, we have divided VIPERS very reliable galaxies (flag 3 and 4) according to the amplitude of the Balmer break and [OII] flux. Table 7 shows the $D4000_n$ and [OII] flux limits we have used for each group, as well as the number of spectra pertaining to that group. We have stacked together the rest frame spectra within each group, and the result is shown in Figure 17. These kind of high quality observed spectra of galaxies at medium redshift can be useful in cross-correlation algorithms, in conjunctions with or alternative to synthetic templates or the classical low redshift templates from Kennicutt (1992), and for this reason we include them in the distributed products. More detailed studies of the spectroscopic properties of VIPERS galaxies making use of stacked spectra are currently ongoing.

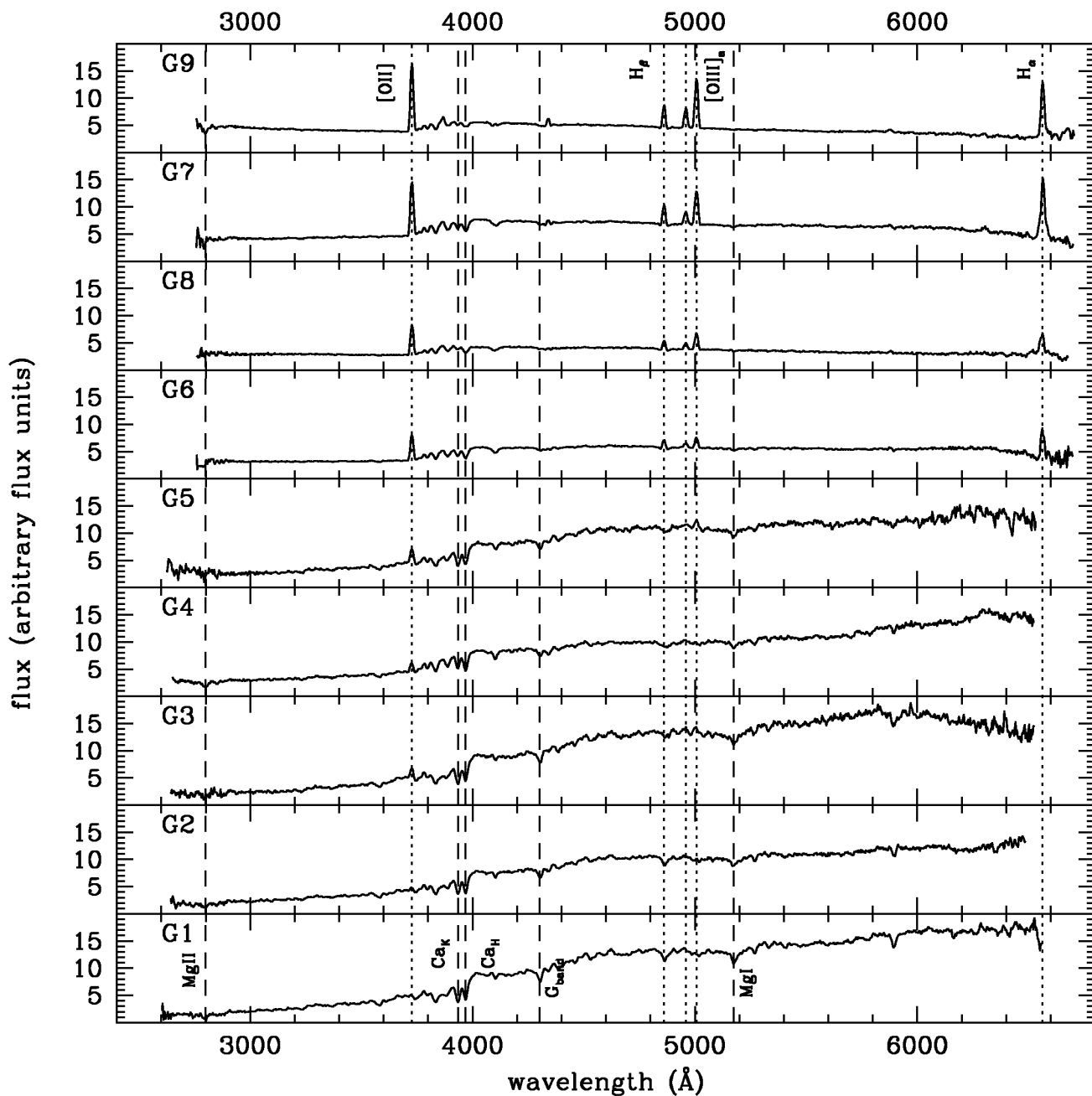


Fig. 17. VIPERS rest-frame stacked spectra for different galaxy groups according to spectral feature strength. Vertical lines indicate location of the strongest features, dotted for emission and dashed for absorption lines.

8. Public Data Release and Database Access

The dataset of the first VIPERS Public Data Release (PDR-1) is available at <http://vipers.inaf.it>. The release comprises:

- **Spectroscopic catalogue.** For each spectroscopically detected source, this catalogue contains: identification (VIPERS internal ID and IAU conventional name), celestial coordinates, selection magnitude, observation epoch, redshift and redshift flag, flag indicating whether the objects is within the photometric mask, Target Sampling Rate and Spectroscopic Success Rate (see 6). The Colour Sampling Rate is provided in analytical form in Equation 9.

- **Parent photometric catalogue.** This table contains all sources in the CFHTLS catalogue falling within the surveyed area and having $i_{AB} < 24.0$. For each source the table gives: VIPERS identification, celestial coordinates, CFHTLS *ugriz* magnitudes, selection magnitude, galactic extinction, half light radius, two flags indicating whether the object is within or outside the photometric and spectroscopic mask flag (see 6). In Guzzo et al. (2013), we have explained that our initial colour selection was based on the CFHTLS-T005 release, and therefore they are included in the release. With CFHTLS-T007 now available, we have added them to the photometric catalogue for convenience.

- **Photometric and survey masks**, as described in Guzzo et al. (2013), in the form of *ds9 region files*.
- **Quadrant dependent TSR and SSR** as described in 6, is the form of ASCII tables.
- **Stacked spectra**, as shown in 7.3, in both ASCII and fits format.

A detailed description of each quantity is provided in the distributed catalogues. We note that with respect to the data used in previous VIPERS papers, in PDR-1 $\sim 0.5\%$ of the redshifts have changed due to a deeper look into the more problematic spectra. As a consequence, for this release we have re-computed also the TSR, SSR and CSR. However we underline that these differences are too small to affect the scientific results contained in previous papers.

A full release of the one dimensional fully calibrated spectra, together with the spectroscopic features measurements, is foreseen in 2014.

Catalogues are distributed in three different forms:

- A single tar file containing the full release
- A web interface connected to the VIPERS database (free registration required), which allows to perform SQL selections through an ergonomic, easy to use interface
- At a later stage, data will also be queryable via the Virtual Observatory

9. Summary

We have presented here the first first Public Data Release (PDR-1) of the VIPERS survey, which includes 57 204 spectroscopic measurements of galaxies, AGN and stars. Complementing the general description given in Guzzo et al. (2013), we have discussed the details of the target selection, observations, data reduction and redshift measurements, providing all relevant information for a proper use of the data. This includes the photometric and angular selection functions, as well as the weighting schemes to be adopted to correct for the survey incompleteness.

Both internal tests and comparison with external redshifts indicate a high reliability of the bulk of the VIPERS redshift data: redshifts classified as Flags 3 and 4 (33 102 objects) in our internal grading system show a confidence level of 99% in their value, while that of the combined Flags 2 and 9 (49 087 objects) is $> 90\%$. Using more than 1500 objects with repeated observations, we have estimated a redshift *rms* error of $0.00047(1+z)$ and shown that this value does not vary significantly along the different Flag classes considered as reliable (i.e. 2, 3, 4 and 9). The overall stellar contamination of the galaxy target sample is found to be smaller than 3%, confirming the goodness of our original star-galaxy separation.

To provide hints on the global spectroscopic quality of the VIPERS data, we have presented first measurements of some basic spectral features, as the Balmer break index and the strength of the [OII] $\lambda 3727$ line. We have also included first comparisons of these spectroscopic markers of mean stellar age and star formation rate to galaxy classification schemes used in other VIPERS papers. This clearly shows the huge potential of this data set for statistical studies of the galaxy population at an average redshift $z \sim 0.8$, an epoch where VIPERS (already with this PDR-1), provides a significant leap in terms of number of galaxies and volume.

The full spectroscopic catalogues, together with the complementary photometric information, survey masks and weights

are publicly available from <http://vipers.inaf.it>. A full release of the corresponding PDR-1 spectra is planned to take place in 2014.

Acknowledgements. We acknowledge the crucial contribution of the ESO staff in the management of service observations. In particular, we are deeply grateful to M. Hilker for his constant help and support of this programme. Italian participation in VIPERS has been funded by INAF through PRIN 2008 and 2010 programmes. LG and BRG acknowledge support of the European Research Council through the Darklight ERC Advanced Research Grant (# 291521). OLF and LAMT acknowledge support of the European Research Council through the EARLY ERC Advanced Research Grant (# 268107). Polish participants have been supported by the Polish National Science Centre (grants N N203 51 29 38 and 2012/07/B/ST9/04425), the Polish-Swiss Astro Project (co-financed by a grant from Switzerland, through the Swiss Contribution to the enlarged European Union), the European Associated Laboratory Astrophysics Poland-France HECOLS and a Japan Society for the Promotion of Science (JSPS) Postdoctoral Fellowship for Foreign Researchers (P11802). GDL acknowledges financial support from the European Research Council under the European Community's Seventh Framework Programme (FP7/2007-2013)/ERC grant agreement n. 202781. WJP and RT acknowledge financial support from the European Research Council under the European Community's Seventh Framework Programme (FP7/2007-2013)/ERC grant agreement n. 202686. WJP is also grateful for support from the UK Science and Technology Facilities Council through the grant ST/I001204/1. EB, FM and LM acknowledge the support from grants ASI-INAF I/023/12/0 and PRIN MIUR 2010-2011. YM acknowledges support from CNRS/INSU (Institut National des Sciences de l'Univers) and the Programme National Galaxies et Cosmologie (PNCG). CM is grateful for support from specific project funding of the *Institut Universitaire de France* and the LABEX OCEVU. The TOPCAT software (Taylor 2005) has been widely used for this paper.

References

- Abazajian, K., Adelman-McCarthy, J. K., Agüeros, M. A., et al. 2003, *AJ*, 126, 2081
- Arnouts, S. & Ilbert, O. 2011, LePHARE: Photometric Analysis for Redshift Estimate, astrophysics Source Code Library
- Balogh, M. L., Morris, S. L., Yee, H. K. C., Carlberg, R. G., & Ellingson, E. 1999, *ApJ*, 527, 54
- Bel, J., Marinoni, C., Granett, B., et al. 2013, *A&A*, submitted
- Bottini, D., Garilli, B., Maccagni, D., et al. 2005, *PASP*, 117, 996
- Colless, M., Dalton, G., Maddox, S., et al. 2001, *MNRAS*, 328, 1039
- Cool, R. J., Moustakas, J., Blanton, M. R., et al. 2013, *ApJ*, 767, 118
- Davidzon, I., Bolzonella, M., Coupon, J., et al. 2013, *A&A*, 558, A23
- de la Torre, S., Guzzo, L., Peacock, J. A., et al. 2013, *A&A*, 557, A54
- Fritz, A., Scoddeggio, M., Ilbert, O., et al. 2013, *A&A*, submitted
- Garilli, B., Fumana, M., Franzetti, P., et al. 2010, *PASP*, 122, 827
- Garilli, B., Le Fèvre, O., Guzzo, L., et al. 2008, *A&A*, 486, 683
- Garilli, B., Paioro, L., Scoddeggio, M., et al. 2012, *PASP*, 124, 1232
- Goranova, Y., Hudelot, P., Magnard, F., et al. 2009, http://terapix.iap.fr/cpl/table_syn_T0006.html
- Granett, B. R., Guzzo, L., Coupon, J., et al. 2012, *MNRAS*, 421, 251
- Guzzo, L., Scoddeggio, M., Garilli, B., et al. 2013, *ArXiv e-prints*
- Hammersley, P., Christensen, L., Dekker, H., et al. 2010, *The Messenger*, 142, 8
- Home, K. 1986, *PASP*, 98, 609
- Ilbert, O., Arnouts, S., McCracken, H. J., et al. 2006, *A&A*, 457, 841
- Kennicutt, Jr., R. C. 1992, *ApJS*, 79, 255
- Le Fèvre, O., Cassata, P., Cucciati, O., et al. 2013, *ArXiv e-prints*
- Le Fèvre, O., Saisse, M., Mancini, D., et al. 2003, in *Proceedings of the SPIE*, ed. M. Iye & A. F. M. Moorwood, Vol. 4841, 1670–1681
- Le Fèvre, O., Vettolani, G., Garilli, B., et al. 2005, *A&A*, 439, 845
- Lilly, S. J., Le Brun, V., Maier, C., et al. 2009, *ApJS*, 184, 218
- Lilly, S. J., Le Fèvre, O., Renzini, A., et al. 2007, *ApJS*, 172, 70
- Malek, K., Solarz, A., Pollo, A., et al. 2013, *A&A*, 557, A16
- Marchetti, A., Granett, B. R., Guzzo, L., et al. 2013, *MNRAS*, 428, 1424
- Marulli, F., Bolzonella, M., Branchini, E., et al. 2013, *A&A*, 557, A17
- Pierre, M., Chiappetti, L., Pacaud, F., et al. 2007, *MNRAS*, 382, 279
- Scoddeggio, M., Franzetti, P., Garilli, B., Le Fèvre, O., & Guzzo, L. 2009, *The Messenger*, 135, 13
- Scoddeggio, M., Franzetti, P., Garilli, B., et al. 2005, *PASP*, 117, 1284
- Taylor, M. B. 2005, in *Astronomical Society of the Pacific Conference Series*, Vol. 347, *Astronomical Data Analysis Software and Systems XIV*, ed. P. Shopbell, M. Britton, & R. Ebert, 29
- Xia, J.-Q., Granett, B. R., Viel, M., et al. 2012, *J. Cosmology Astropart. Phys.*, 6, 10

-
- ¹ INAF - Istituto di Astrofisica Spaziale e Fisica Cosmica Milano, via Bassini 15, 20133 Milano, Italy
 - ² INAF - Osservatorio Astronomico di Brera, Via Brera 28, 20122 Milano, via E. Bianchi 46, 23807 Merate, Italy
 - ³ Dipartimento di Fisica, Università di Milano-Bicocca, P.zza della Scienza 3, I-20126 Milano, Italy
 - ⁴ Aix Marseille Université, CNRS, LAM (Laboratoire d'Astrophysique de Marseille) UMR 7326, 13388, Marseille, France
 - ⁵ INAF - Osservatorio Astrofisico di Torino, 10025 Pino Torinese, Italy
 - ⁶ Canada-France-Hawaii Telescope, 65–1238 Mamalahoa Highway, Kamuela, HI 96743, USA
 - ⁷ Aix-Marseille Université, CNRS, CPT (Centre de Physique Théorique) UMR 7332, F-13288 Marseille, France
 - ⁸ Université de Lyon, F-69003 Lyon, France
 - ⁹ INAF - Osservatorio Astronomico di Bologna, via Ranzani 1, I-40127, Bologna, Italy
 - ¹⁰ Dipartimento di Matematica e Fisica, Università degli Studi Roma Tre, via della Vasca Navale 84, 00146 Roma, Italy
 - ¹¹ Institute of Cosmology and Gravitation, Dennis Sciama Building, University of Portsmouth, Burnaby Road, Portsmouth, PO1 3FX
 - ¹² Institute of Astronomy and Astrophysics, Academia Sinica, P.O. Box 23-141, Taipei 10617, Taiwan
 - ¹³ INAF - Osservatorio Astronomico di Trieste, via G. B. Tiepolo 11, 34143 Trieste, Italy
 - ¹⁴ SUPA, Institute for Astronomy, University of Edinburgh, Royal Observatory, Blackford Hill, Edinburgh EH9 3HJ, UK
 - ¹⁵ Institute of Physics, Jan Kochanowski University, ul. Swietokrzyska 15, 25-406 Kielce, Poland
 - ¹⁶ Department of Particle and Astrophysical Science, Nagoya University, Furo-cho, Chikusa-ku, 464-8602 Nagoya, Japan
 - ¹⁷ Dipartimento di Fisica e Astronomia - Università di Bologna, viale Berti Pichat 6/2, I-40127 Bologna, Italy
 - ¹⁸ INFN, Sezione di Bologna, viale Berti Pichat 6/2, I-40127 Bologna, Italy
 - ¹⁹ Institute d'Astrophysique de Paris, UMR7095 CNRS, Université Pierre et Marie Curie, 98 bis Boulevard Arago, 75014 Paris, France
 - ²⁰ Max-Planck-Institut für Extraterrestrische Physik, D-84571 Garching b. München, Germany
 - ²¹ Astronomical Observatory of the Jagiellonian University, Orla 171, 30-001 Cracow, Poland
 - ²² National Centre for Nuclear Research, ul. Hoza 69, 00-681 Warszawa, Poland
 - ²³ Universitätssternwarte München, Ludwig-Maximilians Universität, Scheinerstr. 1, D-81679 München, Germany
 - ²⁴ INAF - Istituto di Astrofisica Spaziale e Fisica Cosmica Bologna, via Gobetti 101, I-40129 Bologna, Italy
 - ²⁵ INAF - Istituto di Radioastronomia, via Gobetti 101, I-40129, Bologna, Italy
 - ²⁶ Università degli Studi di Milano, via G. Celoria 16, 20130 Milano, Italy
 - ²⁷ INFN, Sezione di Roma Tre, via della Vasca Navale 84, I-00146 Roma, Italy
 - ²⁸ INAF - Osservatorio Astronomico di Roma, via Frascati 33, I-00040 Monte Porzio Catone (RM), Italy